Imaging of large-k phonons in InSb

S. E. Hebboul and J. P. Wolfe
Physics Department and Materials Research Laboratory, University of Illinois at Urbana-Champaign, Urbana, Illinois 61801
(Received 31 March 1986)

Acoustic phonons in InSb with wave vectors up to 30% of the zone boundary are observed to propagate ballistically over a 1 mm distance. An incoherent point source of these large-**k** phonons gives rise to a distinct pattern of caustics, as detected by phonon imaging. This phonon-focusing pattern is obtained using a frequency-selective phonon detector—a Pb superconducting tunnel junction which is sensitive to frequencies above 650 GHz. The phonon image for these high-frequency phonons is markedly different from that obtained for longer path lengths using an Al bolometer, in an experiment which emphasizes lower frequencies ($\sim$300 GHz). The dispersive phonon image is compared to Monte Carlo simulations employing various lattice-dynamics models as input. Shell, dipole, rigid, and bond-charge (BCM) models with parameters previously optimized for neutron scattering data each predict quite distinct phonon-focusing patterns. Qualitatively, the BCM model agrees best with the phonon-imaging data; however, no effort has been made to adjust the many lattice-dynamics parameters of each model. The dispersive phonon images are in agreement with a Monte Carlo calculation which includes phonon scattering from isotopic defects. The combined effects of isotope scattering in the bulk crystal and frequency selectivity of the Pb tunnel junction result in a quasimonochromatic subset of detected phonons with a frequency distribution that is relatively independent of the heat-source distribution.

I. INTRODUCTION

Elastic waves of short wavelength are a particularly important probe of the interatomic forces in crystals. Historically, this has been the domain of lattice-dynamics calculations and neutron scattering experiments. Usually, the phonon dispersion relation $\omega(\mathbf{k})$ is experimentally determined along several symmetry directions and fit to various models of interatomic forces. A complementary method for characterizing the propagation of high-frequency phonons is phonon imaging.[1-3] This technique is sensitive to the shapes of the $\omega(\mathbf{k})=$const surfaces in wave-vector space. We report here phonon-imaging experiments on large wave-vector phonons in InSb and a comparison of these results to calculations based on existing lattice-dynamics models.

Phonon imaging requires the ballistic propagation of phonons over macroscopic distances—generally from a movable heat source on one side of the crystal to a fixed detector on the opposite surface. The advantage of this technique is that a continuous variation of phonon propagation directions can be sampled in a single experiment. What is measured are the *intensities* of the ballistic heat pulses arriving at the detector. The relationship between the intensity pattern emitted from a point source and the elastic properties of the crystal is provided by the theory of phonon focusing.[4] Basically, the nonspherical nature of the constant-frequency surface in wave-vector space gives rise to singularities (or caustics) in heat flux. A measurement of the pattern of caustics by phonon imaging reflects the shape of the $\omega(\mathbf{k})=$const (or "slowness") surface. As the wavelength of the phonons begins to approach twice the lattice constant a (i.e., k approaches π/a), the shape of the slowness surface changes. This is the regime of phonon dispersion.

First experiments by Dietsche, Northrop, and Wolfe[5] showed that the pattern of caustics in Ge indeed depend on the frequency of the detected phonons. More recent work by Northrop, Hebboul, and Wolfe[6] demonstrated the focusing of dispersive phonons in GaAs, and showed that, even for mild dispersion, different lattice-dynamics models predicted significantly different phonon-focusing patterns. In those experiments, the phonon wave vectors selected by the detector had a magnitude of 12 to 18% of the Brillouin-zone boundary. In the present experiments on InSb, we observe distinct caustics in phonon flux for phonons with wave vectors which are at *20 to 30% of the zone boundary*. The phonon-focusing pattern associated with these dispersive phonons is markedly different from that of lower frequency, nondispersive phonons. In all three of the above experiments, the detected phonons had frequencies of about 700 GHz, as determined by the Pb superconducting tunnel-junction detector. For InSb, the "softest" of these crystals, this frequency corresponds to a slow transverse wavelength of only 20 to 30 Å.

Monte Carlo simulations are presented here for four different lattice-dynamics models, using the parameters determined from neutron scattering. At the experimental frequencies near 700 GHz, the models show large qualitative differences. At this point we have not attempted to adjust the model parameters to fit the imaging data. We do, however, address the issue of the distribution of frequencies in these phonon-imaging experiments. Recent isotope scattering calculations by Tamura[7] are used in a Monte Carlo simulation to predict the frequency distribution of ballistically transmitted phonons. For the Pb detector response and our experimental crystal thickness (0.5 mm), there is very little variation in the transmitted frequency distribution as the source temperature is increased beyond about 5K. The spread in frequencies is only about 10% of the central frequency.

These calculations suggest that when isotope scattering

is strong, there is no advantage is directly photoexciting the semiconductor—a method previously suggested[8] to enhance the generation of large-wave-vector phonons. Indeed, we also performed photoexcitation experiments on InSb. Direct photoexcitation produces essentially the same caustic pattern as that obtained with metal-film heat sources. Basically, the sharp onset of detector sensitivity and the strong frequency dependence of isotope scattering together produce a rather narrow frequency distribution which gives rise to a well-defined caustic pattern.[5] Monochromatic phonon detectors, therefore, are not essential in these experiments, greatly relaxing a previously anticipated constraint.

II. IMAGING OF DISPERSIVE PHONONS

There are three basic components to any heat-pulse experiment: generation, propagation, and detection of phonons. To observe the ballistic propagation of large-**k** phonons, one must carefully consider each of these following aspects.

(1) *Phonon generation.* A broadband "point" source of incoherent phonons is produced by locally heating a metal film which is evaporated onto the surface of the sample. In our case, the point source is provided by a focused laser beam. The frequency distribution of phonons emitted from a heated metal film, taking into account the acoustic mismatch between the film and crystal, has been examined in detail by Kappus and Weis:[9] a nearly Planckian distribution of phonons is produced. Alternatively, if the incident photon energy $h\nu$ is larger than the band gap of the crystal, direct photoexcitation of the crystal produces nonequilibrium carriers which relax back to their ground state by emission of phonons.[10] Little is known about the resulting frequency distribution; the initial carrier thermalization process involves emission of optical phonons, which subsequently decay to acoustic phonons. At sufficiently early times after excitation, it is reasonable to expect that the instantaneous phonon distribution is richer in short-wavelength phonons than a Planck distribution created with the same excitation energy.

(2) *Ballistic propagation.* Low temperatures are required to avoid phonon-phonon scattering. High-quality crystals are required to avoid impurity and defect scattering. Transition ions with low-lying electronic excited sites, for example, Cr^{3+} in GaAs, strongly scatter large-**k** phonons. Even in pure crystals, there is a basic limitation—phonon scattering from naturally occurring isotopes. Analogous to Rayleigh scattering, the isotopic scattering rate[11] increases as ν^4. The only ways to avoid this constraint are to use isotopically pure crystals or short path lengths.

(3) *Detection.* Sensitive broadband detection is achieved with a bolometer, e.g., a granular Al film biased in temperature at its superconducting transition. To obtain frequency selectivity, superconducting tunnel junctions[12–14] are used. The junction is operated at a temperature well below its superconducting temperature, and incident phonons with energy greater than the superconducting gap, 2Δ, produce a tunneling current. Fabrication problems associated with our requirements are discussed below.

A. Experimental details

A basic phonon-imaging setup is described in detail in Ref. 3. The objective is to map the spatial distribution of phonon flux emanating from a point source. In the present experiments, we use high-quality undoped InSb samples.[15] These crystals were grown along the [110] symmetry direction by the liquid encapsulation (LCE) method. They contain an impurity concentration of about 7×10^{13} cm^{-3} and have a mobility of 6×10^5 cm^2/V sec at 77 K. A wafer with (110) faces is mechanically polished on both sides using a fine cloth covered with an alumina suspension.[16] The crystals are chemically etched in 1 part nitric acid and 10 parts lactic acid for about 6 min to eliminate damage caused by mechanical polishing.[17] Next, a 2500-Å film of Cu is evaporated on one face of the crystal for phonon generation via laser excitation. Then, a 200-Å layer of SiO is deposited on the opposite face to electrically insulate the detector from the sample. Finally, either an Al bolometer or a Pb-PbO-Pb tunnel junction is fabricated on top of this film.

InSb has very small electron band-gap and effective masses, leading to small donor binding energies and degenerate electron statistics even for small impurity levels. Our samples are sufficiently conducting at 2K to shunt the detectors, thus requiring an insulating film. The SiO layer, however, must be thin enough to allow the transmission of high-frequency phonons. A continuous film of about 200 Å is found to be the smallest practical thickness to ensure insulation. Empirically, we find that depositing this silicon monoxide layer in two 100-Å steps, separated by a 10-min exposure to atmosphere, reduces the potential for shorts. Thicker films resulted in degraded high-frequency phonon signals for the Pb tunnel-junction detectors. The adhesion of evaporated Pb films to SiO is poor, but a procedure which seemed to improve this adhesion was to "flash" deposit about 5 Å of Sn on top of the SiO layer.[18]

Small detectors are required to resolve the angular distribution of phonon flux emitted by a localized source. Both the Al bolometer and the Pb-tunnel-junction detectors were fabricated with an effective sensitive area of about 30×30 μm^2. The Al bolometer is made by vacuum depositing about 600 Å of pure Al through a mask at 10 Å/sec in an oxygen atmosphere of about 3×10^{-5} Torr. The resulting Al strip has a weak link, as shown in Fig. 1(a), which is fine tuned to its superconducting transition by applying a small d.c. current. Typically, the resulting granular Al strip undergoes a superconducting transition between 1.7 and 2.0 K which is higher and broader than that of pure Al films ($T_c=1.2$ K). The resistance curve of the bolometer used to obtain the phonon image of Fig. 2(b) is shown in Fig. 1(a). The 10—90 % width of the superconducting transition is about 0.2 K and permits the detection of minute temperature rises.

Lead tunnel junctions, which detect only phonons whose energies exceed twice the superconducting gap of lead ($2\Delta=650$ GHz), are needed to discriminate against the large flux of lower-frequency phonons. Small, high-quality junctions are difficult to make, because the leakage current generally increases with decreasing area. The Pb tunnel junction consists of two superimposed Pb films

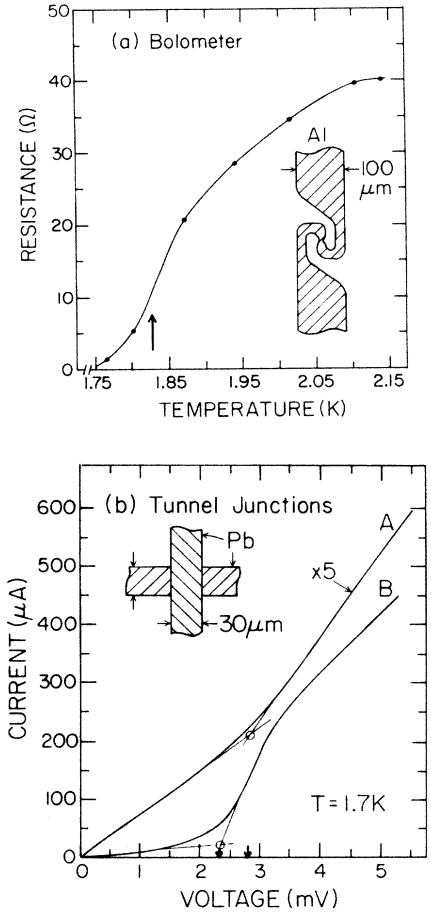

FIG. 1. Operating characteristics of detectors used in the imaging experiments. (a) Resistance of an Al bolometer. The arrow indicates the operating point, where the slope dR/dT is maximum. Inset: diagram of the Al strip geometry. A weak link produces a very small sensitive area for high angular resolution. (b) I-V characteristics of two Pb tunnel junctions. The bottom layer thickness is about 1000 Å for junction A and 1500 Å for junction B. The superconducting 2Δ gap is estimated by locating the intersection of two tangent lines to the I-V curves. This construction yields about 2.8 mV for junction A and 2.3 mV for junction B. A small current is used to bias the junction for phonon detection. Inset: diagram of the overlap geometry.

separated by a thin PbO layer (10—50 Å). The principle of operation is such that an incident phonon with energy greater or equal to 2Δ breaks a Cooper pair in the first (bottom) Pb superconductor. This process generates two free quasiparticles which can then tunnel through the PbO layer to the second (top) Pb film, and give rise to a detectable electric current. The base electrode of the junction is made by evaporating about 1000 Å of pure lead at 20 Å/sec through a 30-μm-wide slit, onto the SiO layer. The sample is then removed from the evaporator and placed in an oxidation chamber[19] for about 15 min under a controlled flow of oxygen at about 80% humidity. Finally, the Pb counterelectrode (2000 Å) is deposited through the same slit mask rotated 90° so that the sensitive detector area is about 30×30 μm^2. This top Pb layer is evaporated more slowly (10 Å/sec) in order to avoid damaging the thin oxide layer. Characteristic curves for two junctions with different film thicknesses are plotted in Fig. 1(b). Typically, the 2Δ gap deduced from the I-V curves of our junctions is between 2.3 and 2.8 meV, close to the nominal gap for a large-area junction, 2.63 meV (650 GHz). High resistance ratios are possible with larger area detectors, with substrates whose thermal expansion coefficient is better matched to Pb films, and with increased thickness of the base Pb electrode. However, we find that a tunnel junction with thicker base electrode is not as efficient a detector of large-$\mathbf{k}$ phonons. Apparently, a thinner base Pb film permits a better penetration of small-wavelength phonons to the junction.

More importantly, we find that while the heat-pulse signal-to-noise ratio depends on the particular characteristics of the junction, the phonon-focusing pattern does not change significantly, even for I-V characteristics as different as the two shown in Fig. 1(b). This implies that the junction sensitivities have a sharp onset at a frequency close to the gap of Pb, regardless of the leakage current or resistance ratio.

B. Experimental results

Two basic experiments are performed to examine nondispersive and dispersive phonon propagation. The first configuration, shown in Fig. 2(a), uses a 2-mm-thick crystal and an Al bolometer to emphasize the low-frequency regime (see Sec. IV.) A relatively broad boxcar gate is used to include ballistic pulses with velocities spanning both slow transverse (ST) and fast transverse (FT) modes. The delay of the time gate after the laser pulse is continuously adjusted to be proportional to the ballistic path length for each source position (i.e., a "sliding gate" or "constant-velocity" mode). The resulting phonon image is displayed in Fig. 2(b). As usual, the most intense regions define a pattern of caustics which is related to the acoustic slowness surface.[1] For comparison, we plot in Fig. 3 the caustic pattern predicted for the low-frequency (continuum) limit, using the low-temperature elastic constants of InSb from acoustic measurements,[20] $C_{11}:C_{12}:C_{44}::1.000:0.545:0.446$. The similarity of this "singularity map" with the phonon image indicates that the detected phonons have little dispersion.

The second configuration, shown in Fig. 2(c), uses a 0.5-mm-thick crystal and a Pb tunnel junction to emphasize phonon frequencies above 650 GHz. A strikingly different phonon image is obtained, as shown in Fig. 2(d). The FT "ridge" structure (center of image) has expanded by nearly a factor of 4, and the ST "diamond" structures centered about the $\langle 100\rangle$ directions have completely changed shape. These radical changes signify a distortion in the slowness surface, which is expected as $\mathbf{k}$ begins to approach the Brillouin-zone boundary.

An important feature in the tunnel-junction image is that rather sharp and distinct features are observed, indicating that the ballistic phonons belong to a slowness surface of well-defined shape. In the dispersive regime, this implies that a relatively monochromatic subset of pho-

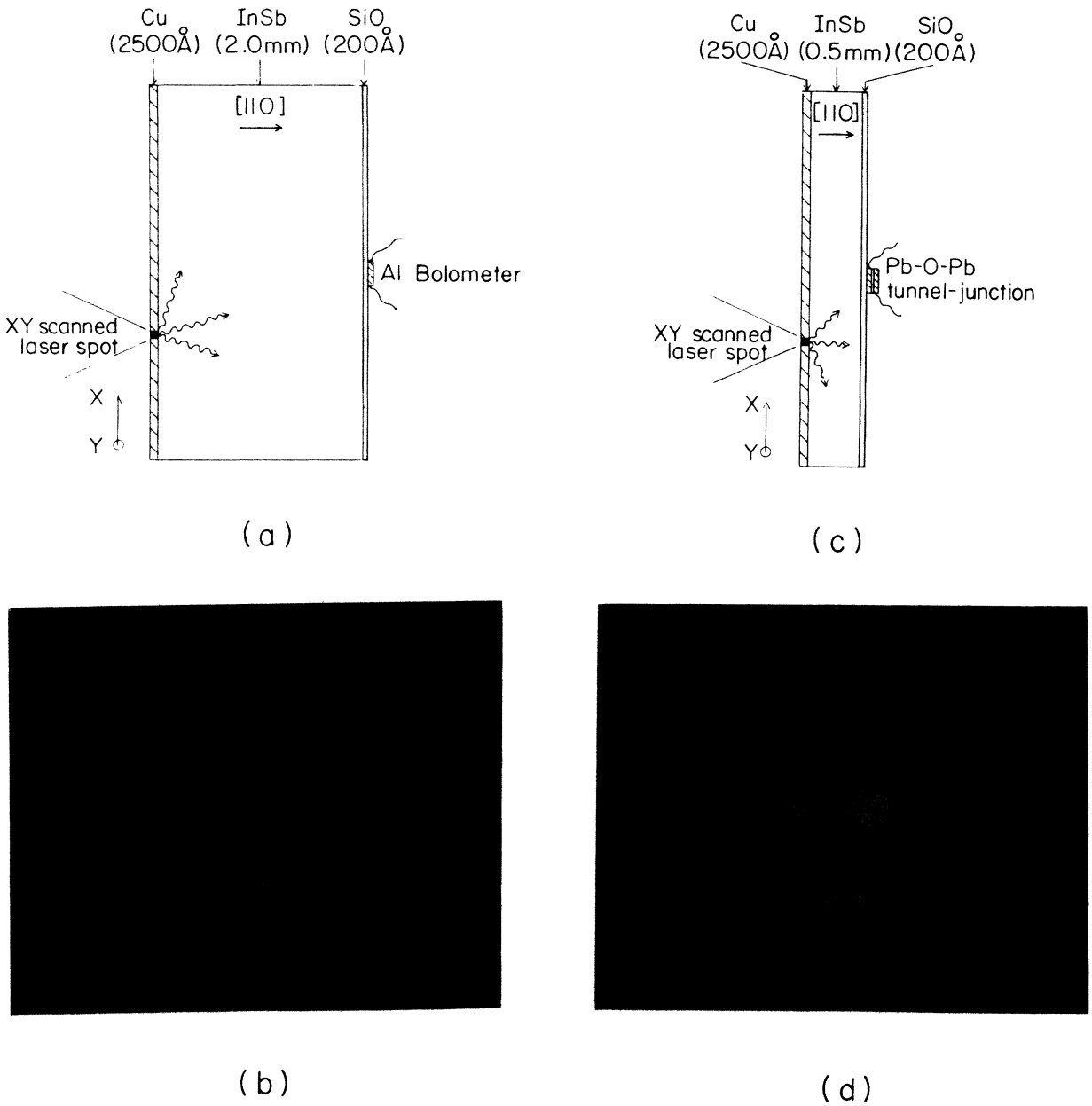

FIG. 2. Phonon images for both the nondispersive and dispersive regimes. (a) Experimental configuration which uses an Al bolometer and a relatively thick crystal (2 mm) to emphasize low-frequency nondispersive phonons. (b) Ballistic phonon image obtained for the configuration in (a) and with the Al bolometer whose characteristics are given in Fig. 1(a). Bright regions correspond to high phonon flux impinging on the (110) face of the crystal. (c) Experimental configuration which uses a relatively thin crystal (0.5 mm) and a Pb tunnel junction to detect high-frequency dispersive phonons. (d) Dispersive phonon image obtained for the configuration in (c) and with junction *A* of Fig. 1(b). Large shifts in the focusing pattern, compared to (b), are attributed to dispersion. The white crosses in the images indicate ⟨111⟩ directions. Those in (d) are determined from Fig. 7.

nons is being observed. This may seem surprising at first, because the tunnel junction is sensitive to all phonons *above* 650 GHz; however, as we will discuss later, isotope scattering inhibits the propagation of very high-frequency phonons, limiting the detected frequencies to a small range above the gap.

The contrast of the phonon-focusing features can be improved by digitally processing the image to account for finite experimental resolution. The laser spot and detector each have a spatial resolution of about 30 μm. Thus, we Fourier transform the 256×256 image, divide out the Fourier transform of a Gaussian with 45-μm full-width at half-maximum (FWHM), and Fourier transform the result back to real space. The deconvolved image, shown in Fig. 4, shows an improvement in contrast and sharpness over the raw data. Well-defined caustics are visible.

At this point we must address the issue of time selection. The heat pulses arriving at the tunnel junction are

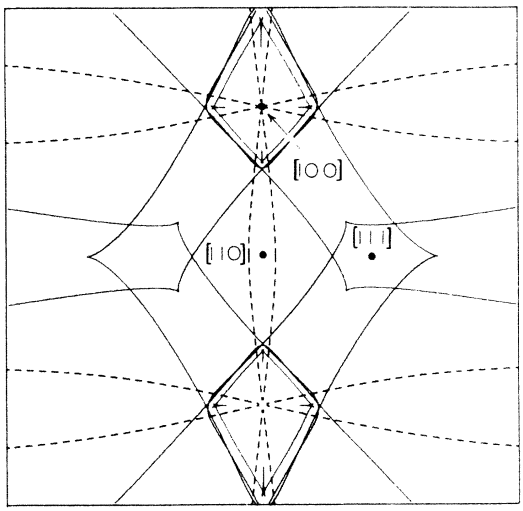

FIG. 3. Calculated phonon-focusing caustics using continuum theory. The low-temperature elastic constants of InSb are taken from Ref. 20. Solid lines are for ST phonons and the dashed lines are for FT phonons. The solid circles locate the intersection of the three symmetry directions with the (110) plane.

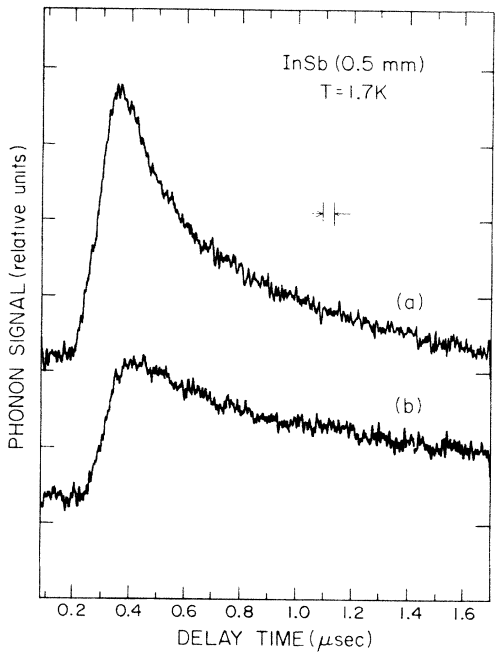

FIG. 5. Heat-pulse traces recorded near the [110] direction by a single Pb tunnel-junction detector placed on a crystal whose excitation face is half covered with a thin copper film: (a) excitation by laser heating the metal film, and (b) direct photoexcitation of the bare crystal ($\lambda = 514.5$ nm). Both excitation methods yield the same spatial pattern shown in Fig. 2(d).

observed to be much broader than the laser pulse width (100 nsec). Typical time traces are plotted in Fig. 5 for two situations—one with a copper generator film (as for the images shown) and one without. Both cases show long tails but the heat pulse generated with a metal film is more peaked near the onset. As the delay of the boxcar gate is adjusted, the intensities of the caustics change but their angular positions remain fixed. The fact that sharp features are observable at up to two or three times the ballistic time of flight indicates that there is a relatively long-lived localized source of phonons at the excitation region. Both photoexcitation and metal-film cases show qualitatively identical focusing patterns, but the metal-film case yields phonon images with higher contrast (better signal-to-noise ratio)—suggesting a more localized source of phonons in that case.

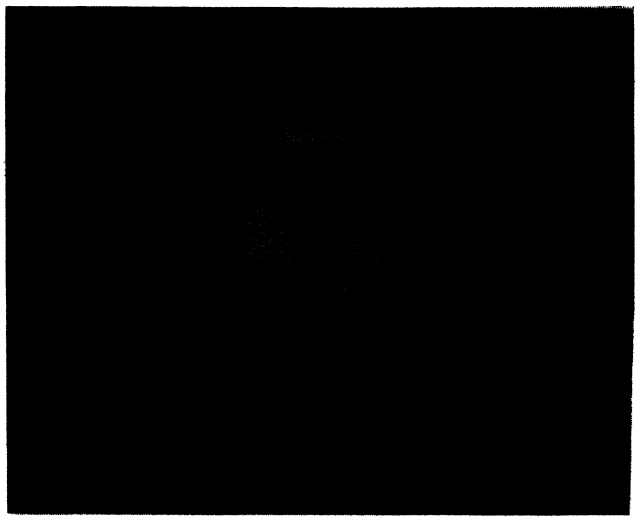

FIG. 4. Spatially filtered image of the dispersive phonon pattern shown in Fig. 2(d). The effective spatial broadening due to source and detector sizes is modeled by a Gaussian of width equal to about 45 μm. After digitally deconvolving this Gaussian from the original image, the image gains sharpness and contrast. The crosses indicate $\langle 111 \rangle$ directions, as determined from Fig. 7.

There is, however, an interesting feature in the phonon image that occurs most prominently at the earliest time delays. A hint of this structure is present in Fig. 4: inside the broad FT ridge appears another weak pair of FT caustics. This structure is more readily seen at early delay times, when the broad ridge is weaker. Figure 6(a) illustrates this case. The phonons associated with this weaker FT structure have larger velocities and lower frequencies. We believe that these weaker signals are due to the tunnel junction acting slightly as a bolometer. The thermally generated junction current is modulated slightly by the large flux of low-frequency phonons. Notice also that the image in Fig. 6(a) shows two superimposed ST structures: the square structure corresponding to ~ 700 GHz and a round structure from lower-frequency phonons. Figure 6(b), obtained with later delay times, illustrates the dominance of the 700-GHz structure when these more dispersive (lower velocity) phonons are selected. The data in Fig. 6 was obtained with junction *B* in Fig. 1(b).

In the images shown so far, there is little evidence of ST focusing structures near $\langle 111 \rangle$. As we will see from Monte Carlo calculations, the intensity of these structures is predicted to be much weaker. To experimentally bring

out these features, we choose longer delay times—corresponding to longer path lengths and slower velocities—and we digitally deconvolve a Gaussian of 60 μm width. This value is found to give the most image contrast, which reasonably suggests a source spreading at later times. Also we average together all four quadrants of the image, making use of the fourfold symmetry to increase the signal-to-noise ratio by a factor of 2. The result

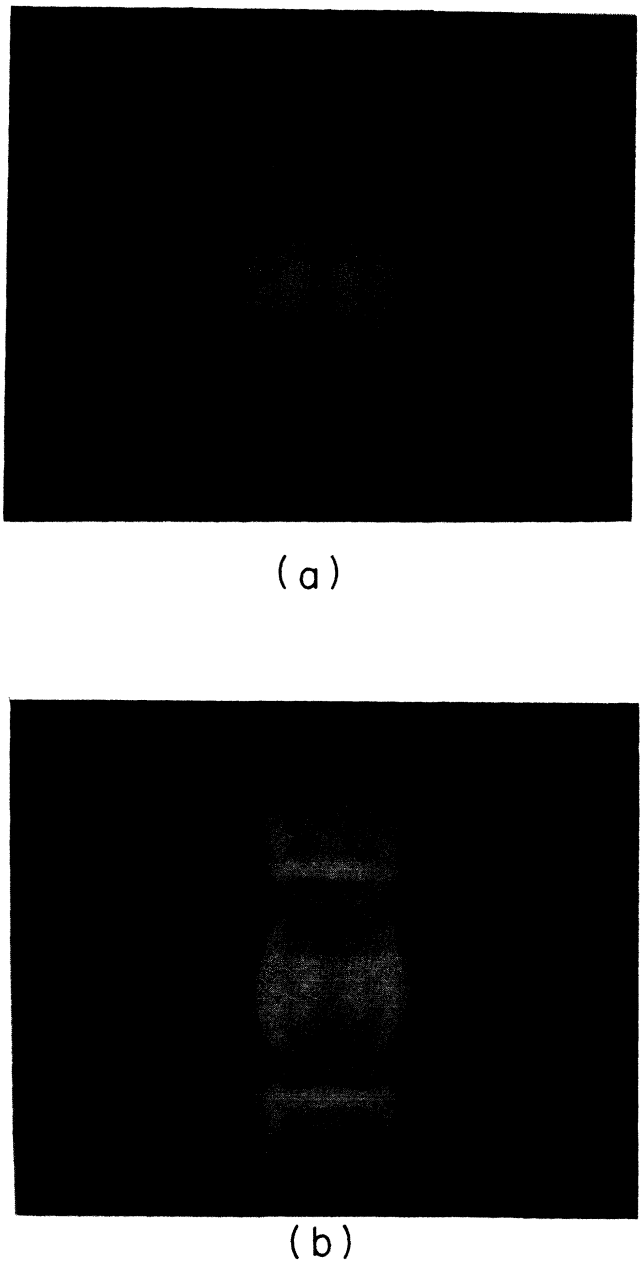

FIG. 6. Dispersive phonon images obtained with Pb tunnel junction B of Fig. 1(b) for a 0.5-mm-thick crystal. Both images are spatially sharpened by deconvolving a Gaussian width of about 45 μm. (a) Early times: a narrow boxcar time gate is adjusted to select a group velocity of about 1.7×10^5 cm/sec. The distinct caustics, characterized by the inner FT ridges and the round ST structure centered about [100], are due to phonons whose average frequency is lower than the 2Δ gap (see text). (b) Later times: same as (a) except sampling a lower group velocity, $V=1.4\times10^5$ cm/sec. The pattern associated with 2Δ phonons is dominant.

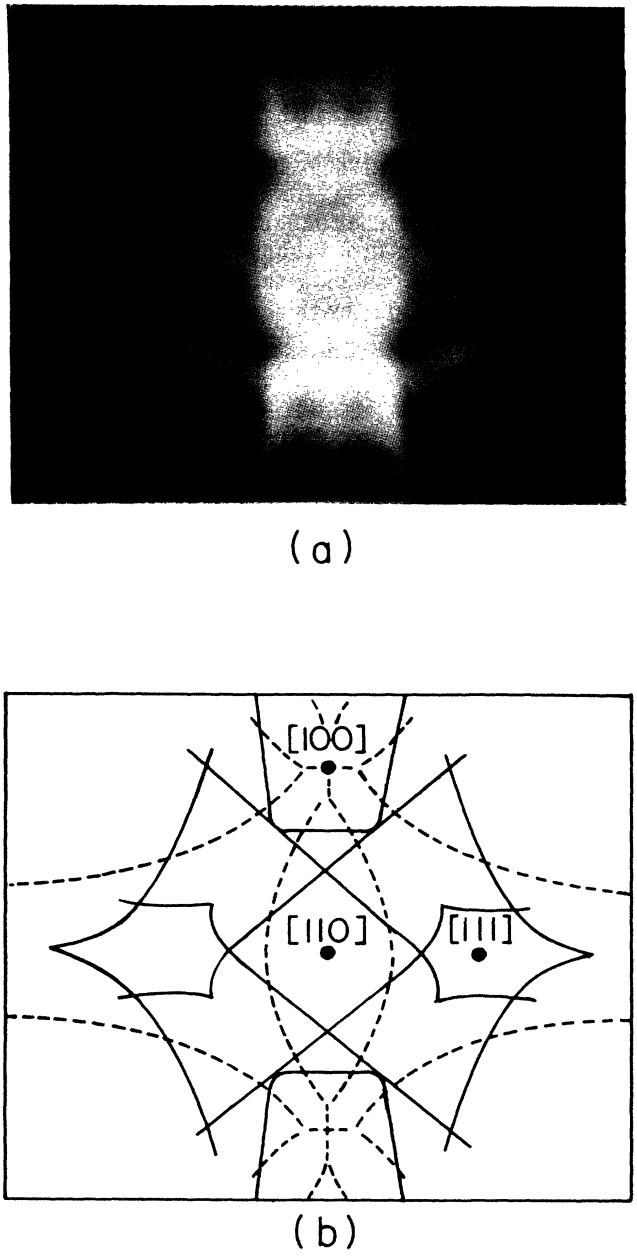

FIG. 7. (a) Processed phonon image obtained with Pb tunnel junction A of Fig. 1(b) for a 0.5-mm-thick crystal. The image is taken at later boxcar delay times and a 60-μm-width Gaussian is then deconvolved to emphasize the weaker ST focusing structures near $\langle 111\rangle$. Also, the four image quadrants are averaged together to increase signal-to-noise ratio by a factor of 2. (b) The positions of the local intensity maxima in (a) are traced from the image to indicate the positions of the caustics. Solid lines are for the ST mode and dashed lines are for the FT mode.

is shown in Fig. 7(a). The threefold-cusp structure about ⟨111⟩ can now be seen. In Fig. 7(b) we sketch the apparent positions of the caustics and indicate the crystalline symmetry directions. Our next task is to compare these results with theoretical calculations.

III. CALCULATIONS OF DISPERSIVE PHONON FOCUSING

For InSb, there is about 30% variation in the sound velocity with propagation direction. Consequently, a phonon's group velocity vector is not, in general, parallel to its wave vector. It is this property of solids which gives rise to the phonon-focusing effect[4] and leads to highly anisotropic phonon-flux distributions. Since phonons travel along the direction of their group velocity, the theoretical problem consists of mapping the group velocity corresponding to an isotropic distribution of phonon wave vectors. Mathematically, the group velocity $\mathbf{V}$ is related to the phonon wave vector $\mathbf{k}$ via the relation

$$\mathbf{V}=\nabla_{\mathbf{k}}\omega(\mathbf{k}) . \quad (1)$$

This equation provides the basis for phonon-focusing calculations in both dispersive and nondispersive regimes. For each phonon frequency ω_0, there is one frequency surface per mode in $\mathbf{k}$ space, given by $\omega_0=\omega(\mathbf{k})$. In general, these constant-frequency surfaces have the shape of deformed spheres. Since group velocity vectors extend along surface normals, it is possible to have a situation in which a large number of phonons with different $\mathbf{k}$ vectors yield nearly a single direction for their group velocities. The phonon flux in that propagation direction is then considerably enhanced. Mathematical singularities in phonon intensity correspond to lines on the surface where the total Gaussian curvature vanishes.[1]

In the long-wavelength limit (i.e., the nondispersive regime), this energy channeling is well predicted in the context of continuum theory of elasticity. Basically, the crystal is treated as a continuous medium whose direction-dependent elastic properties display anisotropies directly related to the fourth-rank elasticity tensor C_{ijlm}. The phase velocity $v=\omega/k$ of mechanical vibrations (phonons) is then found to be independent of the wave-vector magnitude k but varies with direction. As a result, the shape of constant-energy surfaces is independent of frequency.

A. Lattice dynamics

When the wavelength of phonons approaches the size of interatomic spacings, the discrete nature of the crystal has to be taken into account and continuum elasticity theory is no longer valid. The focusing properties of large-$\mathbf{k}$ phonons in Ge (Refs. 5, 21, and 22) and GaAs (Ref. 6) have been previously studied. Because InSb is somewhat softer than these two crystals, a given frequency (700 GHz) gives rise to a much more pronounced effect, as seen in the experimental data.

In order to explain the Pb tunnel-junction data presented in Sec. II microscopic theories which predict wave motion from interatomic forces need to be considered.[23] These lattice-dynamics models are characterized by a set of adjustable parameters. The parameters have been previously varied until the computed dispersion relation $\omega(\mathbf{k})$ along high-symmetry directions best fits existing inelastic neutron scattering measurements for all branches. Acoustic measurements of elastic constants are often used as additional input to the model calculations.

Based on varying assumptions about interatomic forces, several lattice-dynamics models have been applied to III-V compound semiconductors, all of which agree reasonably well with neutron scattering data. In this paper, we report calculations for InSb which are performed with four of the most commonly used models. Briefly, the models are (1) a 15-parameter deformation-dipole model[24–26] using static charges, atomic deformabilities, local polarizabilities, and coupling parameters extending to second-nearest neighbors; (2) an 11-parameter rigid-ion model[24–26] obtained by setting the local polarizabilities to zero in the dipole model; (3) a 10-parameter valence-force-field shell model[27,28] which views the atoms as having ionic cores and rigid, displaceable electronic shells, and describes core-core, core-shell, and shell-shell interactions to second-nearest neighbors; and (4) a 6-parameter adiabatic bond-charge model[29,30] (BCM) characterized by interactions involving massless bond charges which are allowed to move adiabatically. Given an arbitrary wave vector $\mathbf{k}$, each model provides $\omega(\mathbf{k})$ as an input to our phonon-focusing calculations. No attempt has been made to adjust any of the published model parameters to fit our phonon-focusing results.

Dispersion curves for the TA branch in the [100] and [111] propagation directions, as predicted by each model, are shown in Fig. 8 along with neutron scattering mea-

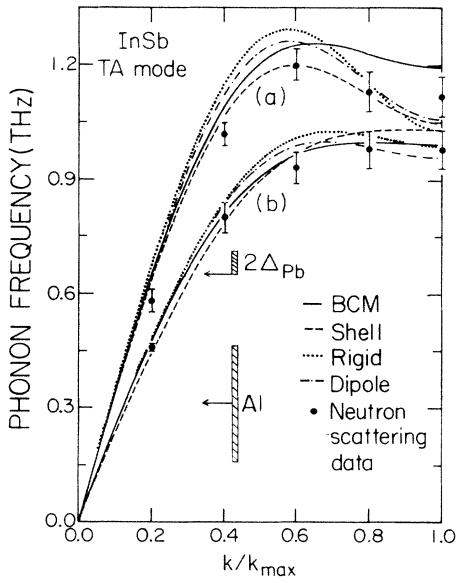

FIG. 8. Dispersion curves $\omega(\mathbf{k})$ for the TA modes of InSb along two symmetry directions: (a) [100] propagation and (b) [111] propagation, as calculated by BCM, shell, rigid, and dipole models. Neutron scattering measurements are taken from Ref. 31 and shown with the experimental error bars. The computed frequency distribution widths of heat pulses detected by Al and Pb detectors are represented by vertical bars (see Sec. IV). The arrows locate frequency distribution maxima.

surements[31] for InSb. The model fitting procedure (not ours) includes the neutron scattering data in the [100], [110], and [111] symmetry directions for all phonon branches. In this case, the four models fall fairly close to the experimental error bars in the [111] direction, whereas more serious deviations occur along the [100] direction for these acoustic branches. In general, differences among models become more prominent as **k** approaches the Brillouin zone boundary. The 2Δ gap of our Pb tunnel junctions is indicated in Fig. 8 and the computed frequency range of detected phonons which are transmitted through a 0.5-mm-thick InSb crystal is shown as a vertical bar (see Sec. V). Similarly, the computed frequency range for phonons transmitted through a 2-mm-thick sample and detected by a broadband Al bolometer is shown. The arrows locate the peaks for both distributions.

To see how well these lattice-dynamics models predict phonon focusing, it is useful to plot $\omega(\mathbf{k})$ at a constant frequency. The curves in Fig. 9 represent the intersections of slowness surfaces [$\omega(\mathbf{k})=\omega_0$ surfaces] with a (110) plane, which contains all three high-symmetry directions. As the phonon frequency increases, the constant-frequency surfaces distort differently for each model. Inflection points where the local curvature vanishes are

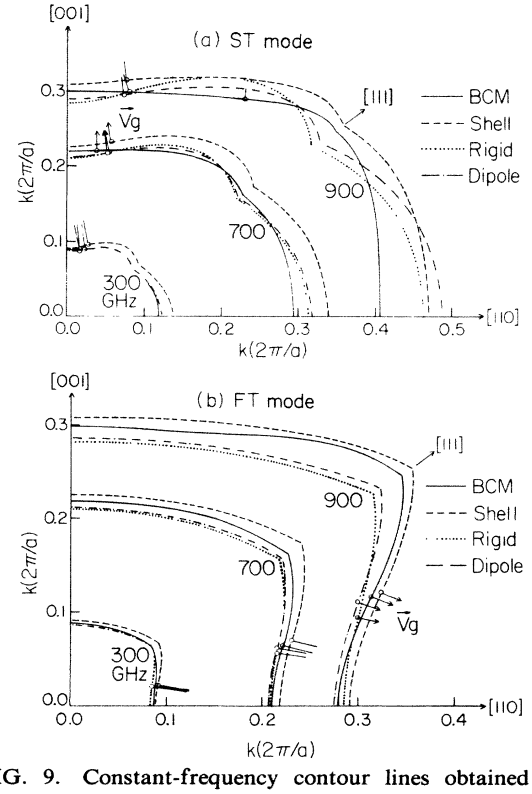

FIG. 9. Constant-frequency contour lines obtained when slowness surfaces at 300, 700, and 900 GHz intersect a (110) plane, as predicted by BCM, shell, rigid, and dipole models for InSb. (a) ST mode and (b) FT mode. Circles mark inflection points which lead to phonon-flux singularities along group velocity vectors $\mathbf{V}_g$ at those points. Dispersion causes these constant-frequency surface to distort and results in a substantial shift in the focusing pattern. For a given frequency, the models predict different shapes for the slowness surface and consequently yield different focusing patterns.

represented by open circles. Large phonon intensities are predicted along the direction of surface normals, or group velocities, at these inflection points. For example, the angle that the group velocity vectors make with the [110] direction in Fig. 9(b) corresponds to half the angular width of the FT "ridge," as illustrated with the dashed lines in Fig. 3. All four models predict that the angle increases with frequency, in agreement with experiment. However, each model yields a different value for this angle [Fig. 9(b)]. Consequently, dispersive phonon imaging appears to be a very sensitive tool in evaluating the relative merit of lattice-dynamics models in predicting the acoustic modes, because it provides a direct handle on the curvature of constant-frequency surfaces. Similar remarks can be made about the ST focusing features.

B. Monte Carlo simulations

Phonon-focusing patterns associated with each lattice-dynamics model are produced by assuming an initial random but isotropic distribution of wave vectors **k** and mapping them into real space using Eq. (1). Each phonon contributes to the brightness of the image pixel corresponding to its particular propagation direction in the experimental plane. Monte Carlo images for each of the four above-mentioned lattice-dynamics models are shown in Fig. 10.

In order to produce these clear phonon-focusing patterns, approximately 10^6 **k** vectors need to be processed. Since, depending on the lattice-dynamics model, it takes anywhere from 0.5 to about 30 sec of central processing unit (cpu) time to map one phonon on a VAX 750 computer, direct computation is impractical. Instead, we resort to a "neighborhood Monte Carlo" scheme to simulate the phonon-flux patterns.[3,6] First, the symmetry-reduced section of the Brillouin zone is divided up into about 10^4 cells, and $\omega(\mathbf{k})$ is determined at the center of each cell. Coefficients for a second-order Taylor expansion of $\omega(\mathbf{k})$ are determined at each point, which provides an efficient **k** to **V** mapping of all wave vectors in the neighborhood of that point. Determining the array and local expansion coefficients requires about 3—70 h of cpu time. A large number of randomly selected wave vectors can then be converted to group velocity vectors and mapped onto the experimental plane, where their density represents phonon flux. Next, we calculate Monte Carlo phonon-focusing patterns by imposing constraints on ω, **V**, or **k**. This part of the processing is relatively fast; about $\frac{1}{2}$ h of cpu time is required for 10^6 phonon trajectories.

The Monte Carlo images shown in Fig. 10 are produced for the frequency interval 650—750 GHz, to compare with a Pb tunnel-junction data. This range of selected frequencies is justified in Sec. V. For each model, both the ST and FT phonon modes are displayed in the same image. Significant variations are apparent among the models. For example, the widths of the FT ridges (center of pattern) vary by a factor of about 1.5. More striking, however, are the differences in the shapes and sizes of the ST focusing structures around the ⟨100⟩ directions. The BCM model predicts a pattern in Fig. 10(d) which is qual-

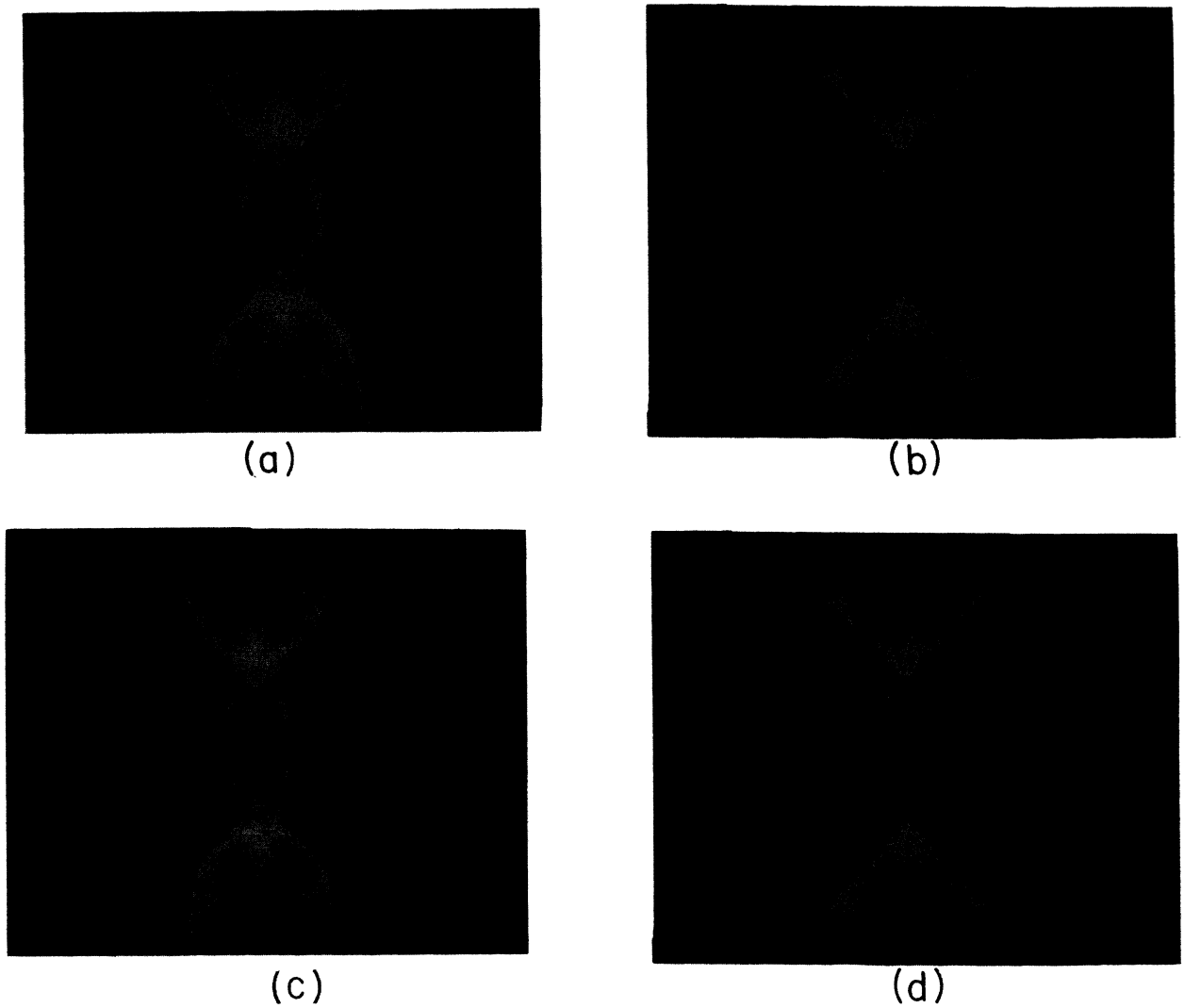

FIG. 10. Calculated phonon-focusing patterns for the frequency range 650—750 GHz using four lattice-dynamics models: (a) shell, (b) rigid, (c) dipole, and (d) BCM. These are to be compared with Pb tunnel-junction data presented in Figs. 2(d) and 7.

itatively the most similar to the Pb tunnel-junction data (Fig. 7). Dipole and rigid models yield markedly different ST structures around the [100] direction even though their associated contour lines in Fig. 9(a) almost coincide at 700 GHz. This demonstrates the sensitivity of phonon-focusing structures to small differences in the curvatures of the constant-frequency surfaces.

Next we illustrate the frequency-dependence of the phonon-flux distributions. Figure 11(a) is a Monte Carlo simulation using the continuum-limit elasticity tensor. Figures 11(b) and (c) show the focusing patterns produced with the BCM model for the frequency intervals 250—350 and 850—950 GHz, respectively. The focusing pattern of Fig. 11(c) is due to dispersive phonons which lie deep in the Brillouin zone at about $0.5k_{\max}$. Figure 11(b) is in good qualitative agreement with the Al bolometer data of Fig. 2(b), but the sizes of the structures do not match exactly. Even at frequencies as low as 300 GHz, therefore, a significant effect of dispersion on the phonon-focusing pattern of InSb can be observed.[32]

IV. FREQUENCY DISTRIBUTION OF THE BALLISTIC PHONONS

The elastic scattering rate of a phonon traveling through an isotopically impure crystal increases as the fourth power[11] of its frequency ν, that is, $\tau^{-1}=A\nu^4$. The attenuation coefficient, $e^{-RA\nu^4/V}$, represents the probability that a phonon with frequency ν and group velocity V propagates ballistically a distance R. This isotope scattering can be incorporated into our Monte Carlo calculations as follows.

(1) A phonon wave vector $\mathbf{k}$ is selected at random as before and its corresponding frequency $\nu(\mathbf{k})$ and group velocity $\mathbf{V}=2\pi\nabla_{\mathbf{k}}\nu(\mathbf{k})$ are obtained by the linear interpolation method described above, using a given lattice-dynamics model.

(2) The isotope scattering rate is computed using Tamura's low-frequency-limit expression[7] $\tau_{\text{InSb}}^{-1}=(1.62\times10^{-41})\nu^4$ sec^{-1}, which is assumed to hold throughout the 0—1000 GHz range.[33]

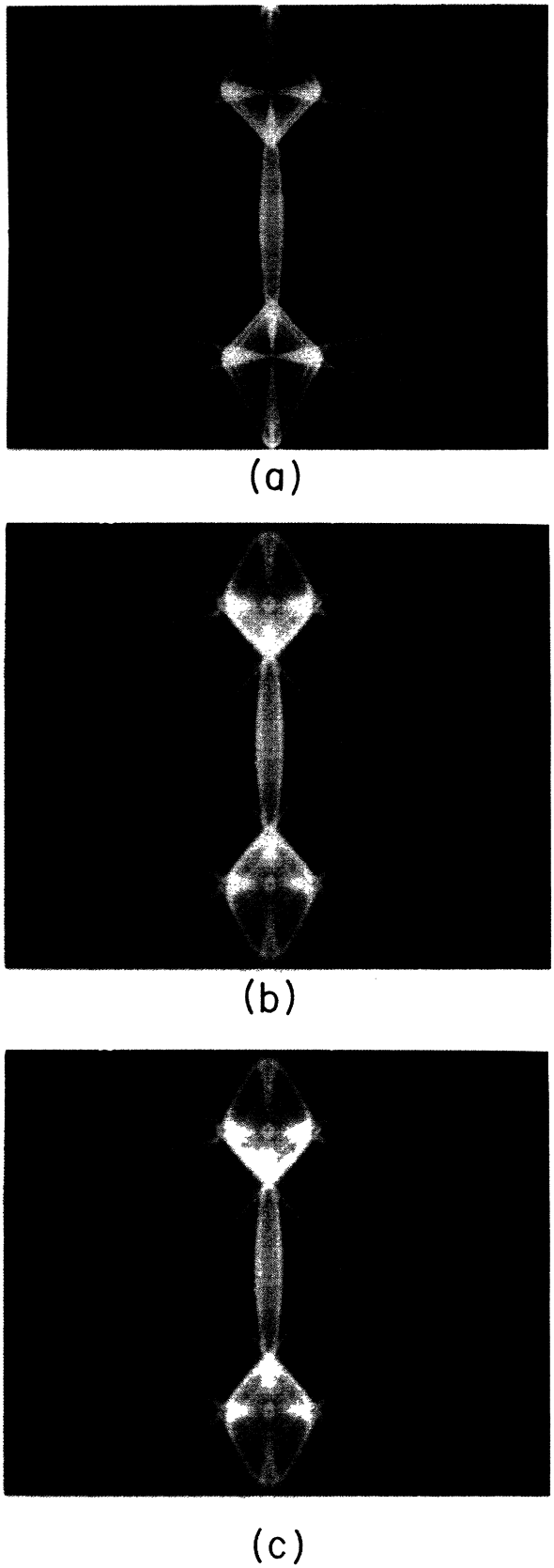

FIG. 11. Frequency dependence of the computed phonon-flux patterns. (a) Elasticity theory, $\nu \approx 0$ GHz. The elastic constants are taken from Ref. 20. (b) BCM, $\nu = 250-350$ GHz, and (c) BCM, $\nu = 850-950$ GHz.

(3) The transmission probability $e^{-R/V\tau}$ is evaluated, and a point is added to the image with this probability. In effect, phonons which scatter are ignored and ballistic phonons are tabulated.

The frequency distribution of transmitted phonons originating from a selected initial phonon distribution can now be investigated theoretically. In particular, a Planck spectrum is known to describe the frequency distribution of phonons emitted from heated metal films.[34] The results of calculations using the bond-charge model (BCM) are shown in Fig. 12 assuming an initial 10-K Planck distribution. The small circles in Fig. 12(a) and 12(c) represent the number of ST phonon counts tabulated at 25-GHz intervals, summed over all propagation directions. The initial Planck distribution is obtained by setting the crystal thickness to $d = 0$ mm, which eliminates the effects of isotope scattering in the computation.

We consider two particular situations, corresponding to the two experimental images in Fig. 2. The calculation of Fig. 12(a) is for a 2-mm-thick crystal with a broadband detector. The transmission factor assuming a single nondispersive velocity[34] $V_{ST}[110] = 1.68 \times 10^5$ cm/sec is plotted for comparison. The transmitted distribution, however, is calculated using the actual dispersive velocity for each phonon. We see that the combined effects of dispersion, $V(\nu)$, and varying path lengths, R, pull the transmitted distribution slightly towards smaller frequencies and allow fewer phonons, especially in the high-frequency region, to follow a collision-free path to the other side of the crystal. The corresponding image of ballistically transmitted phonons is printed in Fig. 12(b). The result is similar to the data of Fig. 2(b).

In the second calculation, Fig. 12(c), we consider a 0.5-mm-thick crystal and a detector with a sharp onset threshold at 650 GHz ($=2\Delta_{Pb}$). In this case, the combination of detector response and isotope scattering produces a remarkably sharp distribution of transmitted phonons, with a FWHM of only 9% of the center frequency. The calculated image for this distribution is shown in Fig. 12(d). This theoretical image is quite similar to the data of Fig. 4.

So far, we have only discussed the case of an initial Planck distribution which is characterized by a single heater temperature $T = 10$ K. Next, we examine changes in the transmitted phonon distribution as the heater temperature is varied. In Fig. 13(a) are plotted the frequency of the peak (ν_p), the FWHM (Δ) and the "cutoff" frequency (ν_c), all derived from the transmitted distributions as defined in Fig. 12(a). A striking feature is the rapid saturation of the distribution characteristics with increasing heater temperature. This result stresses that isotope scattering acts to severely limit the mean free path of high-frequency, large-k phonons in crystals, regardless of the original form of the phonon distribution. Figure 13(b) shows that the FWHM of the tunnel-junction distribution strongly saturates at about 11% of the gap frequency. We believe that this is why the phonon images using a Pb tunnel junction exhibited essentially the same caustic pattern as when the crystal face was directly photoexcited, i.e., no metal film. Huet and Maneval,[35] however, have observed an upward shift in the transmitted spectrum of LA pho-

nons when the crystal is photoexcited. LA phonons suffer less scattering from isotopes due to their relatively higher sound velocities ($V_L[110]=3.8\times10^5$ cm/sec), and weaker dispersion.

The continuous curves of Fig. 13 are obtained by fitting a simple model which takes into account the experimental geometry. The dispersion relation, $\nu(k)$, is approximated throughout the Brillouin zone by a sinusoidal function whose zone-boundary value is made to coincide with the neutron scattering measurement[31] of 1.12 THz. The transmitted phonon flux is then integrated over the image plane, and the resulting ν_P, $\Delta\nu$, and ν_c of the distribution are plotted against heater temperature. The single fitting parameter is a sound velocity which turns out to be 2.0×10^5 cm/sec, which is close to the average TA velocity[34] at $k=0$.

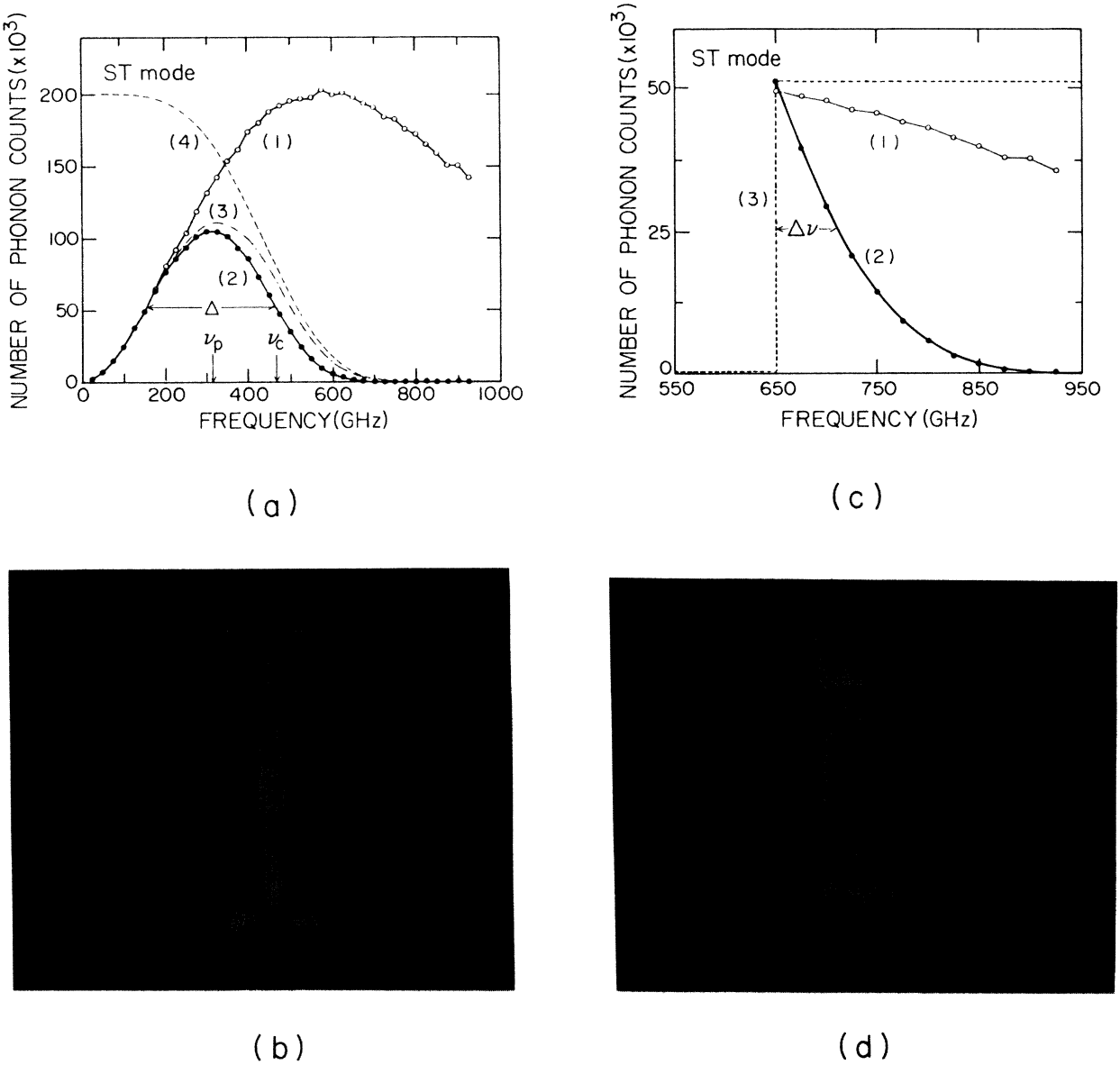

FIG. 12. Predicted frequency distributions of ballistic phonons and their associated focusing patterns when the isotope scattering effect is included. Results are presented for the two types of detector responses: Al bolometer [(a) and (b)], and Pb tunnel junction [(c) and (d)], using BCM. (a) Calculations for a 2-mm-thick InSb crystal: (1) initial 10-K Planck distribution, obtained for a vanishing crystal thickness in the computation, (2) transmitted phonon distribution, (3) transmitted distribution, Planck $\times e^{-d/V\tau}$, along the [110] direction ($d=2$ mm) for a single sound velocity $V_{ST}=1.68\times10^5$ cm/sec (from Ref. 34), and (4) transmission factor, $e^{-d/V\tau}$, in (3). (b) Computed focusing pattern due to the transmitted distribution (2) in (a). (c) Calculations for a 0.5-mm-thick crystal: (1) initial 10-K Planck distribution (divided by 4), (2) transmitted distribution, and (3) ideal Pb tunnel-junction response function with a gap at $2\Delta_{Pb}=650$ GHz. (d) Computed focusing pattern due to the transmitted distribution (2) in (c).

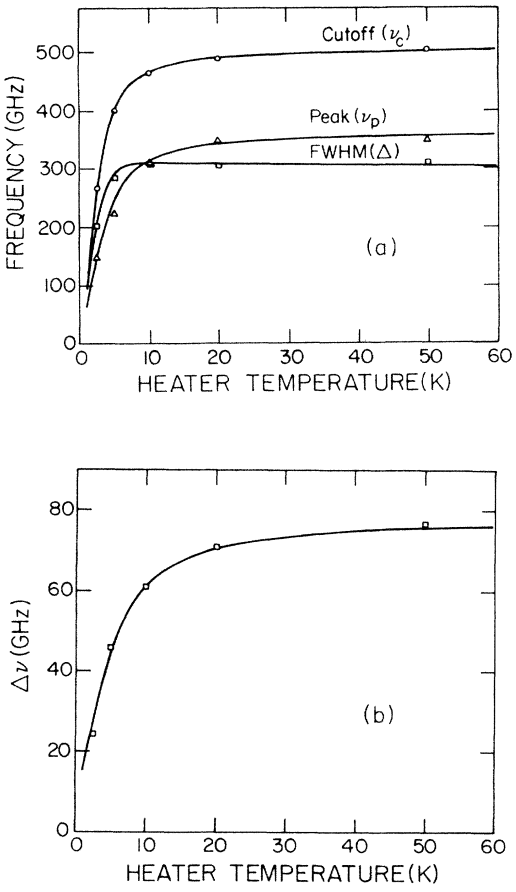

FIG. 13. Dependence of the transmitted phonon distributions in Fig. 12(a) and (c) on heater temperature. Data points are obtained from Monte Carlo calculations as in Fig. 12. The continuous curves are the result of fitting a simple sine-like model for dispersion $\omega(\mathbf{k})$ to the Monte Carlo data. (a) FWHM peak, and cutoff frequencies, as defined in Fig. 12(a), versus heater temperature for Al bolometer response. (b) The width $\Delta\nu$ defined in Fig. 12(c) versus heater temperature for Pb tunnel-junction response.

V. SUMMARY AND PROSPECTS

While much quantitative analysis of dispersive focusing patterns remains, we believe that these experiments on InSb have overcome some major hurdles. Ballistic propagation of acoustic phonons with wave vectors up to 30% of the zone boundary have been observed, and their phonon-focusing pattern is markedly different from that of nondispersive phonons. The sharpness of these dispersive structures and their insensitivity to time selection imply a major simplification in the interpretation of dispersive phonon images: an almost monochromatic set of ballistic phonons is being detected. Our Monte Carlo analyses, making use of Tamura's model for isotope scattering in InSb, show why this is the case. The combination of a detector with sharp frequency onset and isotope scattering acting as a relatively sharp low-pass filter produces a relatively narrow frequency distribution of ballistic phonons ($\Delta\nu/\nu < 10\%$). We have found that direct photoexcitation of the crystal is not necessary, or even desirable, for producing large-**k** phonons (as previously thought): metal-film excitation seems to produce a more localized heat source which is desirable for angular resolution. Therefore, even optically transparent crystals may be studied by this method.

Future experimental directions may include the use of other types of tunnel junctions such as PbBi with $\Delta \simeq 870$ GHz and NbN with $2\Delta \simeq 1$ THz to probe deeper into the Brillouin zone. *In situ* frequency tunability is a real possibility: for example, an external magnetic field can be applied to lower the superconducting gap. In each case, the thickness of a crystal must be chosen with consideration for spatial resolution and phonon scattering lengths.

The analysis of the phonon images is still at an early stage. Methods must be devised to numerically fit a given lattice-dynamics model to a particular phonon image. Presently each model depends on a large number of adjustable parameters. It is possible that data from both neutron scattering measurements (which also contains information on optical branches) and phonon images could be used in obtaining an optimal set of fitting parameters. One way to quantify the phonon images would be to fit them with a phenomenological lattice-dynamics theory, the parameters of which could be incorporated into a particular lattice-dynamics model much as the low-frequency constants are now incorporated. No universal phenomenological theory like continuum mechanics has been developed for a discrete lattice, but progress has been made recently towards that end. DiVincenzo[36] has examined the form of the dynamical matrix in cubic crystals up to second-order in wave vector. So far, his approach should be applicable to mildly dispersive phonons. Obviously, it would be very useful if the positions of the caustics in Fig. 7 could be reproduced using one or two adjustable parameters in the dynamical matrix in addition to the elastic constants.

Despite these technical difficulties, one thing remains clear: the dispersive phonon images of InSb at 700 GHz contain information about the elastic wave surfaces which is not completely accounted for in any of the lattice-dynamics models we used—at least as they are presently fit to the neutron scattering data. BCM, which was actually devised for covalently bonded semiconductors and has the fewest adjustable parameters, best reproduces the qualitative features of the phonon image. It would be interesting, for example, to see if adjustment of the model parameters could provide better agreement with the phonon images without significantly affecting the fit to the neutron scattering data. If so, a more accurate representation of elastic wave propagation in InSb would be achieved.

ACKNOWLEDGMENTS

We are grateful to E. Swiggard of the Naval Research Laboratory who grew the InSb crystals used in our experiments. D. Van Harlingen, W. Dietsche, and G. A. Northrop provided useful advice in the fabrication and operation of the tunnel junctions. We made use of software developed by G. A. Northrop for dispersive pho-

non imaging. Y. C. Chang provided us with the basic programs for BCM. We appreciate the availability of lattice-dynamics calculations by Kunc and Nielson. This research is supported in part by the National Science Foundation under a Materials Research Laboratory Grant No. NSF-DMR-83-16981. Equipment support was provided under the National Science Foundation Grant No. NSF-DMR-80-24000.

[1]G. A. Northrop and J. P. Wolfe, Phys. Rev. Lett. **43**, 1424 (1979); Phys. Rev. B **22**, 6196 (1980).

[2]J. P. Wolfe, Phys. Today **33**(12), 44 (1980).

[3]G. A. Northrop and J. P. Wolfe, in *Proceedings on a NATO Advanced Study Institute of Nonequilibrium Phonon Dynamics, Les Arcs, France 1984,* edited by W. E. Bron (Plenum, New York, 1985).

[4]B. Taylor, H. J. Maris, and C. Elbaum, Phys. Rev. Lett. **23**, 416 (1969).

[5]W. Dietsche, G. A. Northrop, and J. P. Wolfe, Phys. Rev. Lett. **47**, 660 (1981).

[6]G. A. Northrop, S. E. Hebboul, and J. P. Wolfe, Phys. Rev. Lett. **55**, 95 (1985).

[7]S. Tamura, Phys. Rev. B **30**, 849 (1984).

[8]R. G. Ulbrich, V. Narayanamurti, and M. A. Chin, Phys. Rev. Lett. **45**, 1432 (1980).

[9]W. Kappus and O. Weis, J. Appl. Phys. **44**, 1947 (1973); O. Weis, Z. Angew. Phys. **26**, 325 (1969).

[10]R. Orbach, Phys. Rev. Lett. **16**, 15 (1966).

[11]P. G. Klemens, Proc. Phys. Soc. London **68**, 113 (1955).

[12]W. Eisenmenger and A. H. Dayem, Phys. Rev. Lett. **18**, 125 (1967).

[13]A. H. Dayem, B. I. Miller, and J. J. Wiegand, Phys. Rev. B **3**, 2949 (1971).

[14]H. Kinder, in *Proceedings of a NATO Advanced Study Institute on Nonequilibrium Phonon Dynamics, Les Arcs, France, 1984,* edited by W. E. Bron (Plenum, New York, 1985).

[15]The InSb single crystals were provided by E. Swiggard of the U. S. Naval Research Laboratory.

[16]The final step is 0.1 μm CR Alpha, Baikowski International, Co.

[17]This procedure was suggested by Ohio Semitronics, Inc.

[18]R. E. Joynson, in *Handbook of Thin Film Technology,* edited by L. I. Maissel and R. Glang (McGraw-Hill, New York, 1970), pp. 22—32.

[19]J. P. Garno, J. Appl. Phys. **48**, 4627 (1977).

[20]H. J. McSkimin, IRE Trans. Ultrason. Eng. **PGUE-5**, 25 (1957).

[21]G. A. Northrop, Phys. Rev. B **26**, 903 (1982).

[22]S. Tamura, Phys. Rev. B **25**, 1415 (1982); **28**, 897 (1983).

[23]M. Born and H. Kuang, *Dynamical Theory of Crystal Lattices* (Oxford University Press, New York, 1954); M. J. P. Musgrave, *Crystal Acoustics* (Holden-Day, San Francisco, 1970).

[24]K. Kunc, M. Balkanski, and M. A. Nusimovici, Phys. Status Solidi B **71**, 341 (1975).

[25]K. Kunc, M. Balkanski, and M. A. Nusimovici, Phys. Status Solidi B **72** 229 (1975).

[26]K. Kunc and O. H. Nielson, Comput. Phys. Commun. **16**, 181 (1979).

[27]P. H. Borchards and K. Kunc, J. Phys. C **11**, 4145 (1978).

[28]K. Kunc and O. H. Nielson, Comput. Phys. Commun. **17**, 413 (1979).

[29]K. C. Rustagi and W. Weber, Solid State Commun. **18**, 673 (1976).

[30]S. K. Yip and Y. C. Chang, Phys. Rev. B **30**, 7037 (1984).

[31]D. L. Price, J. M. Rowe, and R. M. Nicklow, Phys. Rev. B **3**, 1268 (1971).

[32]We are reminded of the heat-pulse experiments of Huet, Maneval, and Zylbersztejn, Phys. Rev. Lett. **29**, 1092 (1972), which showed a 2% longer time of flight using a Sn tunnel junction ($2\Delta = 280$ GHz) than for an Al bolometer.

[33]Tamura's detailed calculations (see Ref. 7) which take into account dispersion, show that the scattering rate of near zone-boundary phonons increases somewhat more rapidly than predicted by the ν^4 behavior.

[34]D. Huet, B. Pannetier, F. R. Ladan, and J. P. Maneval, J. Phys. (Paris) **37**, 521 (1976).

[35]D. Huet and J. P. Maneval, in *Proceedings of the Third International Conference of Phonon Scattering in Condensed Matter, 1979,* edited by H. J. Maris (Plenum, New York, 1980).

[36]D. P. DiVincenzo, Phys. Rev. B (to be published).

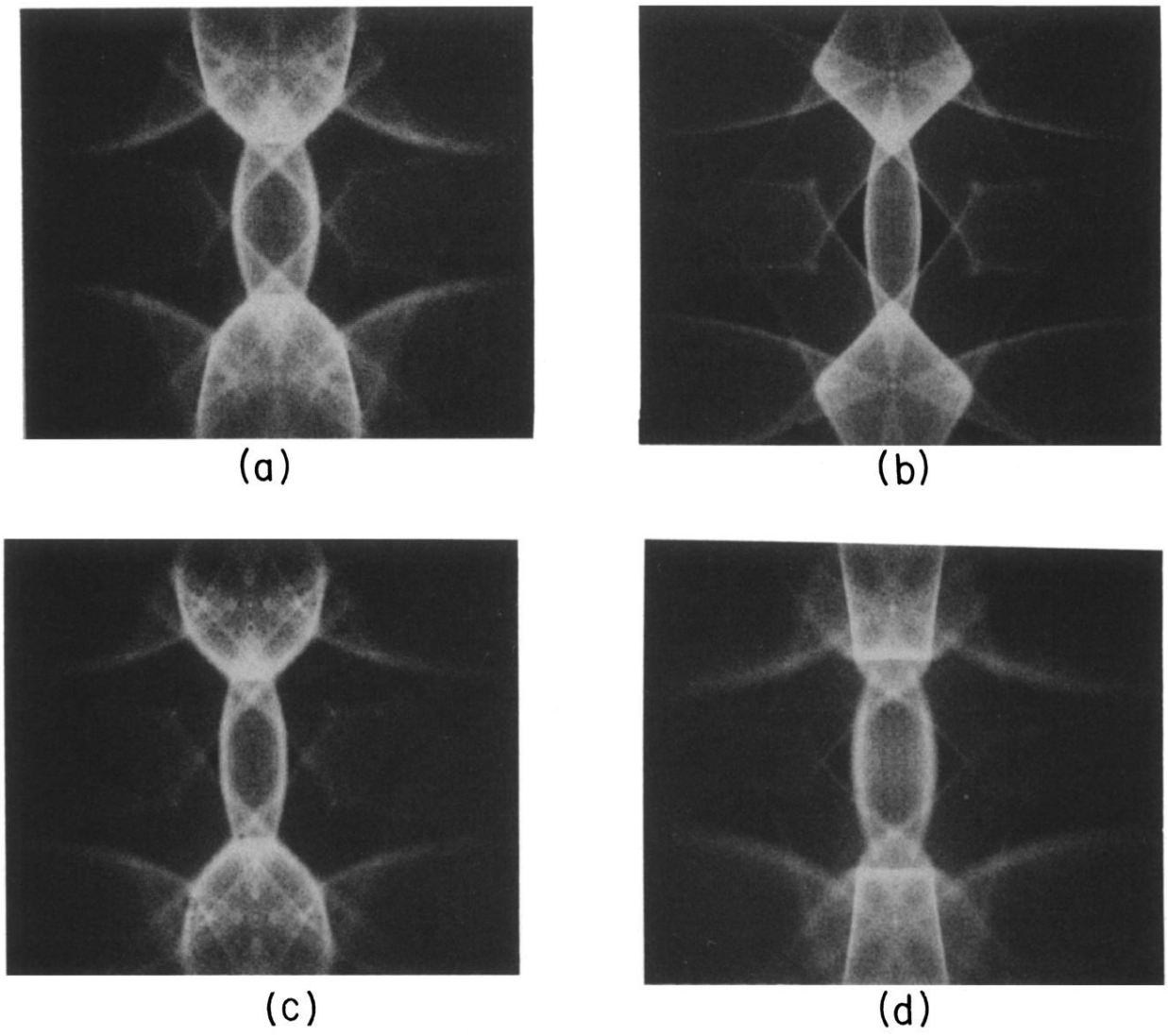

FIG. 10. Calculated phonon-focusing patterns for the frequency range 650—750 GHz using four lattice-dynamics models: (a) shell, (b) rigid, (c) dipole, and (d) BCM. These are to be compared with Pb tunnel-junction data presented in Figs. 2(d) and 7.

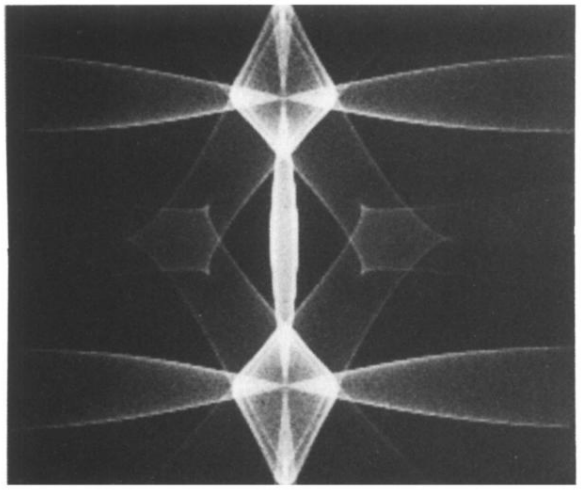

(a)

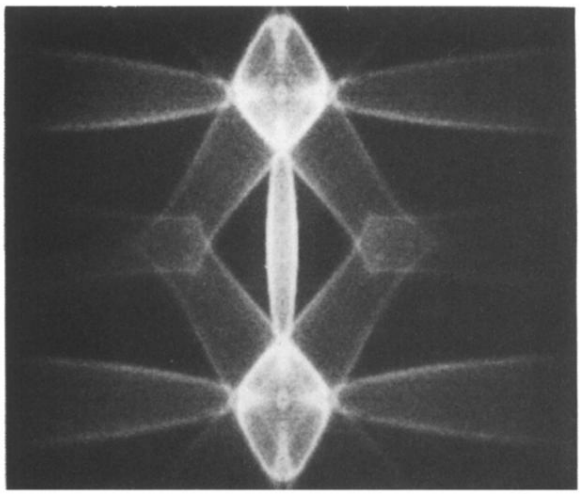

(b)

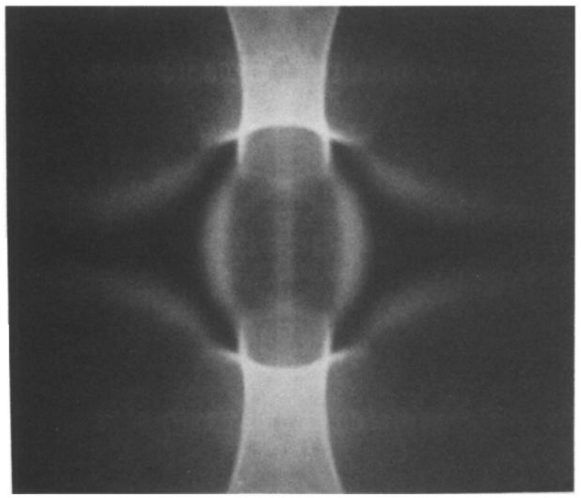

(c)

FIG. 11. Frequency dependence of the computed phonon-flux patterns. (a) Elasticity theory, $\nu \approx 0$ GHz. The elastic constants are taken from Ref. 20. (b) BCM, $\nu = 250$–350 GHz, and (c) BCM, $\nu = 850$–950 GHz.

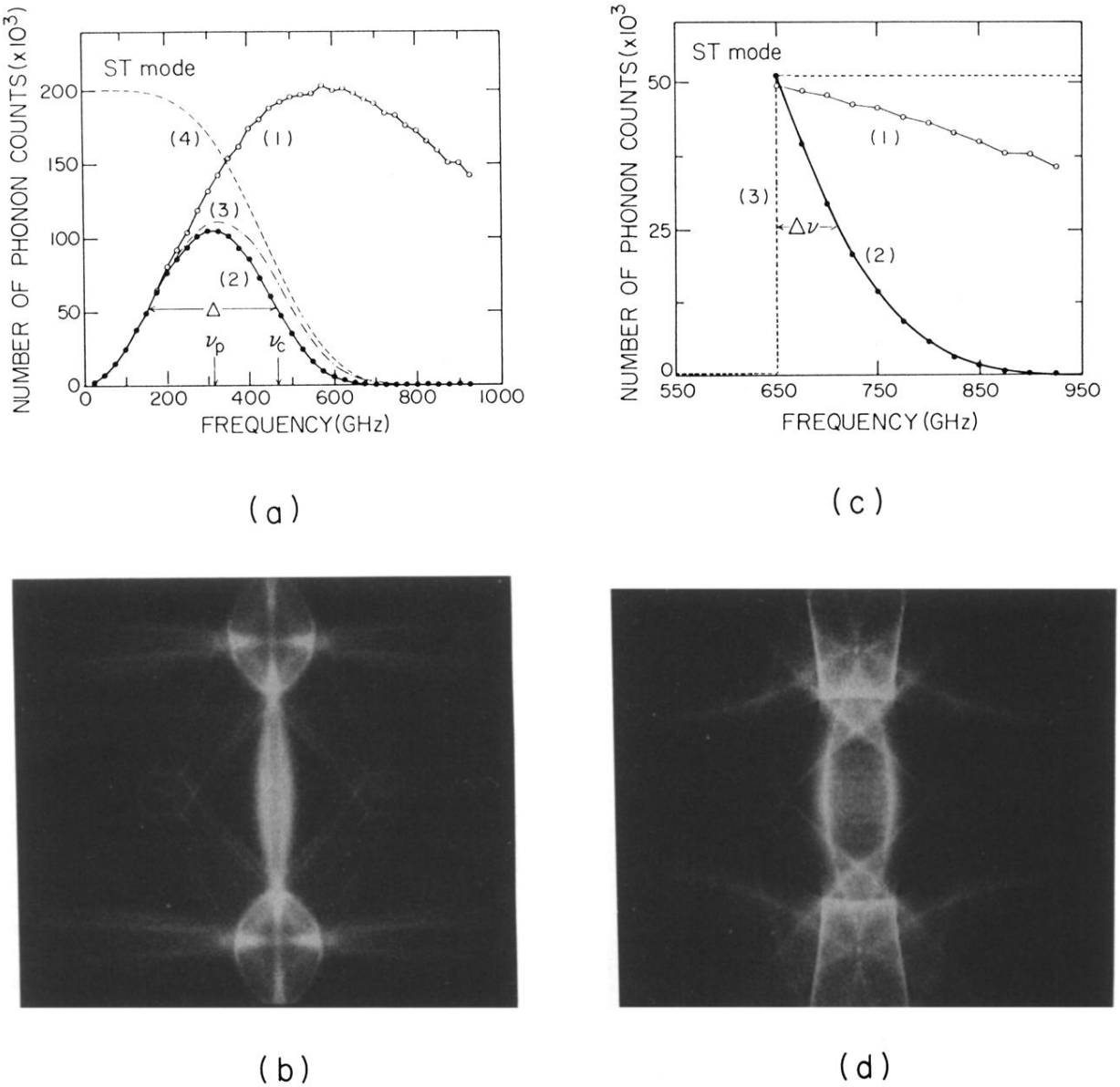

FIG. 12. Predicted frequency distributions of ballistic phonons and their associated focusing patterns when the isotope scattering effect is included. Results are presented for the two types of detector responses: Al bolometer [(a) and (b)], and Pb tunnel junction [(c) and (d)], using BCM. (a) Calculations for a 2-mm-thick InSb crystal: (1) initial 10-K Planck distribution, obtained for a vanishing crystal thickness in the computation, (2) transmitted phonon distribution, (3) transmitted distribution, Planck $\times e^{-d/V\tau}$, along the [110] direction ($d=2$ mm) for a single sound velocity $V_{ST}=1.68\times10^5$ cm/sec (from Ref. 34), and (4) transmission factor, $e^{-d/V\tau}$, in (3). (b) Computed focusing pattern due to the transmitted distribution (2) in (a). (c) Calculations for a 0.5-mm-thick crystal: (1) initial 10-K Planck distribution (divided by 4), (2) transmitted distribution, and (3) ideal Pb tunnel-junction response function with a gap at $2\Delta_{Pb}=650$ GHz. (d) Computed focusing pattern due to the transmitted distribution (2) in (c).

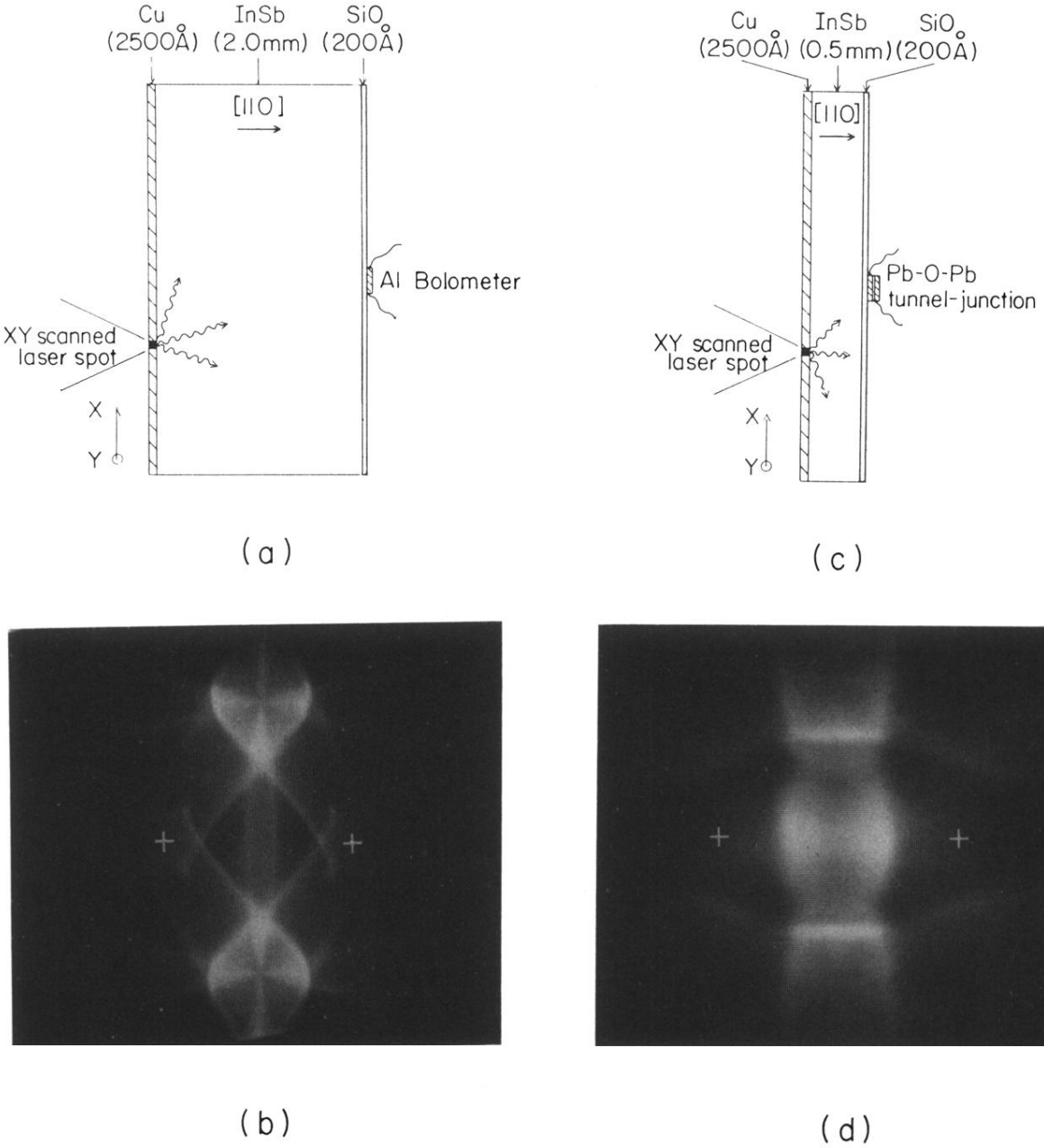

FIG. 2. Phonon images for both the nondispersive and dispersive regimes. (a) Experimental configuration which uses an Al bolometer and a relatively thick crystal (2 mm) to emphasize low-frequency nondispersive phonons. (b) Ballistic phonon image obtained for the configuration in (a) and with the Al bolometer whose characteristics are given in Fig. 1(a). Bright regions correspond to high phonon flux impinging on the (110) face of the crystal. (c) Experimental configuration which uses a relatively thin crystal (0.5 mm) and a Pb tunnel junction to detect high-frequency dispersive phonons. (d) Dispersive phonon image obtained for the configuration in (c) and with junction *A* of Fig. 1(b). Large shifts in the focusing pattern, compared to (b), are attributed to dispersion. The white crosses in the images indicate ⟨111⟩ directions. Those in (d) are determined from Fig. 7.

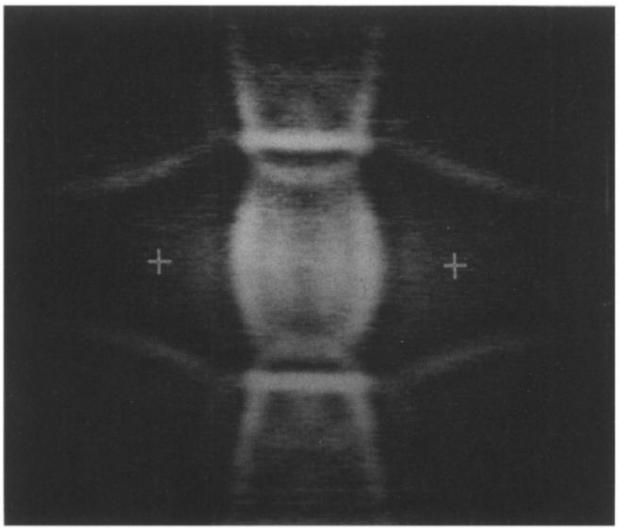

FIG. 4. Spatially filtered image of the dispersive phonon pattern shown in Fig. 2(d). The effective spatial broadening due to source and detector sizes is modeled by a Gaussian of width equal to about 45 μm. After digitally deconvolving this Gaussian from the original image, the image gains sharpness and contrast. The crosses indicate $\langle 111 \rangle$ directions, as determined from Fig. 7.

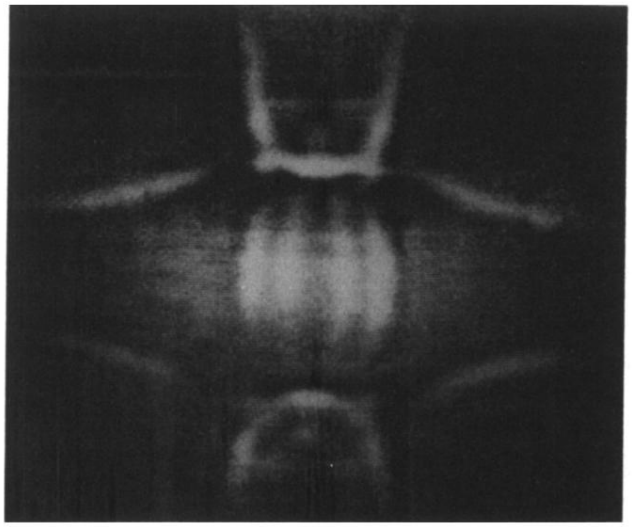

(a)

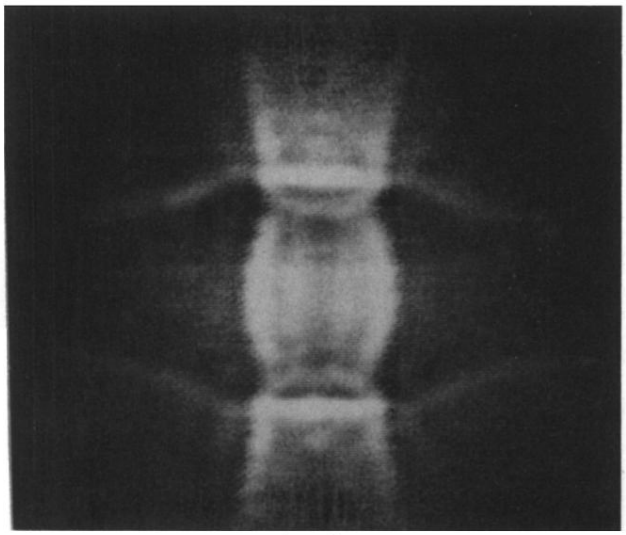

(b)

FIG. 6. Dispersive phonon images obtained with Pb tunnel junction B of Fig. 1(b) for a 0.5-mm-thick crystal. Both images are spatially sharpened by deconvolving a Gaussian width of about 45 μm. (a) Early times: a narrow boxcar time gate is adjusted to select a group velocity of about 1.7×10^5 cm/sec. The distinct caustics, characterized by the inner FT ridges and the round ST structure centered about [100], are due to phonons whose average frequency is lower than the 2Δ gap (see text). (b) Later times: same as (a) except sampling a lower group velocity, $V=1.4\times10^5$ cm/sec. The pattern associated with 2Δ phonons is dominant.

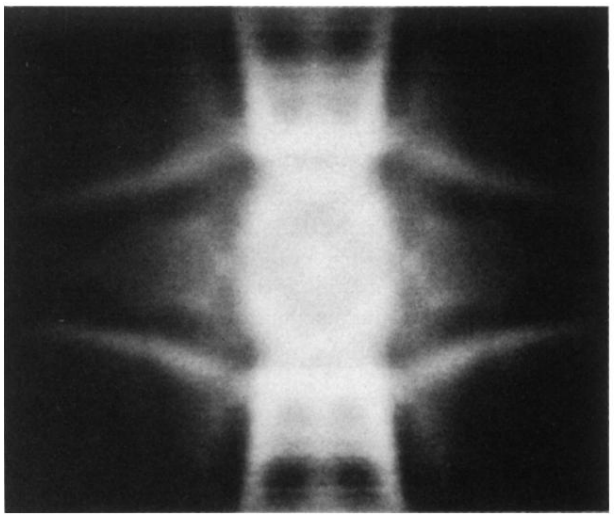

(a)

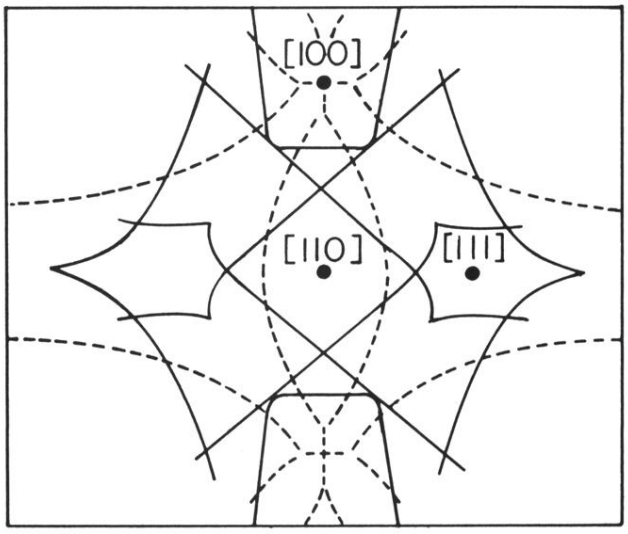

(b)

FIG. 7. (a) Processed phonon image obtained with Pb tunnel junction *A* of Fig. 1(b) for a 0.5-mm-thick crystal. The image is taken at later boxcar delay times and a 60-μm-width Gaussian is then deconvolved to emphasize the weaker ST focusing structures near $\langle 111 \rangle$. Also, the four image quadrants are averaged together to increase signal-to-noise ratio by a factor of 2. (b) The positions of the local intensity maxima in (a) are traced from the image to indicate the positions of the caustics. Solid lines are for the ST mode and dashed lines are for the FT mode.